Journal of Physics and Chemistry of Solids 160 (2022) 110342

Contents lists available at ScienceDirect

Journal of Physics and Chemistry of Solids

journal homepage: www.elsevier.com/locate/jpcs

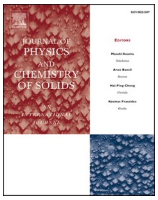

Investigating the effects of various synthesis routes on morphological, optical, photoelectrochemical and photocatalytic properties of single-phase perovskite $BiFeO_3$

Shui-Wen Chang Chien [a], Ding-Quan Ng [a], Dileep Kumar [b,c], Sze-Mun Lam [d,e], Zeeshan Haider Jaffari [a,*]

[a] Department of Environmental Engineering and Management, Chaoyang University of Technology, No. 168, Jifeng E. Rd, Wufeng District, Taichung, 413310, Taiwan
[b] Division of Computational Physics, Institute for Computational Science, Ton Duc Thang University, Ho Chi Minh City, Viet Nam
[c] Faculty of Applied Sciences, Ton Duc Thang University, Ho Chi Minh City, Viet Nam
[d] College of Environmental Science and Engineering, Guilin University of Technology, Guilin, 541004, China
[e] Department of Environmental Engineering, Faculty of Engineering and Green Technology, Universiti Tunku Abdul Rahman, 31900, Kampar, Perak, Malaysia

ARTICLE INFO

Keywords:
$BiFeO_3$
Chemical synthesis
Magnetic
Photoelectrochemical
Photocatalysis

ABSTRACT

Herein, various $BiFeO_3$ morphologies, including sheet-like, coral-like and rod-like structures, were synthesized via co-precipitation (CP), hydrothermal (HT), and sol-gel (SG) synthesis routes, respectively. The as-synthesized samples were characterized by physicochemical techniques to investigate their crystal structure, optical and photoelectrochemical properties. The SG-$BiFeO_3$ sample exhibited remarkable direct sunlight photocatalytic degradation of phenol (98.95%), superior to those of the HT-$BiFeO_3$ (77.4%) and CP-$BiFeO_3$ (66.9%) in 120 min. The SG-$BiFeO_3$ sample was the most effective among all due to the lower energy band gap value and highest separation of photogenerated charge carriers, which was validated by the UV–vis absorption, photoluminescence (PL) and photoelectrochemical measurements. The recycling and ferric (Fe^{3+}) ion leakage test suggested that the SG-$BiFeO_3$ sample was highly stable for up to six consecutive runs. The radical scavenger studies implied that the photogenerated hole (h^+), hydrogen peroxide (H_2O_2) and hydroxyl radicals (•OH) were the dominant reactive species. Finally, based on these, a possible photocatalytic mechanism for phenol degradation over SG-$BiFeO_3$ sample was also postulated.

1. Introduction

Semiconductor photocatalysis, as a non-hazardous and environment-friendly technique, has been widely applied for eliminating environmental contamination as well as the energy crisis [1,2]. To date, numerous semiconductors such as TiO_2, ZnO and CuO have been investigated for the photodegradation of organic contaminants [1,3]. Nonetheless, the practical applications of the photocatalysts as mentioned above are still restricted due to wide bandgap energies and rapid recombination of photogenerated charge carriers [4,5]. To overcome these shortcomings, various attempts, including noble metal doping [6,7], ion substation [8,9] and heterojunction formation [5,10], have been made. All these investigations have achieved substantial progress, yet some intrinsic problems are not entirely resolved. Hence, from the practical application point of view, it is necessary to develop photocatalytic semiconductor materials with smaller energy band gaps and higher charge carrier separation efficiency.

Perovskite bismuth ferrite ($BiFeO_3$) is one of the rare single-phase multiferroic semiconductors which is visible light-responsive due to a small energy bandgap (2.1 eV) [7,11]. Besides, it is non-toxic and has outstanding chemical stability [12]. The low decomposition temperature of bismuth salts makes it difficult to synthesize $BiFeO_3$ material without any impurities using conventional solid-state synthesis process at higher sintering temperatures [13]. Chemical techniques including sole-gel [14], hydrothermal [15], rapid liquid phase sintering [16] and co-precipitation [17] methods have been applied to synthesize $BiFeO_3$ materials with the required morphologies. The photocatalytic applications of these studies suggested that the control over particle size and shape had an important role in the performance due to the influence of bandgap energy and the number of surface reaction sites [18,19].

---

* Corresponding author.
E-mail address: jaffarizh@hotmail.com (Z.H. Jaffari).

https://doi.org/10.1016/j.jpcs.2021.110342
Received 15 June 2021; Received in revised form 5 August 2021; Accepted 15 August 2021

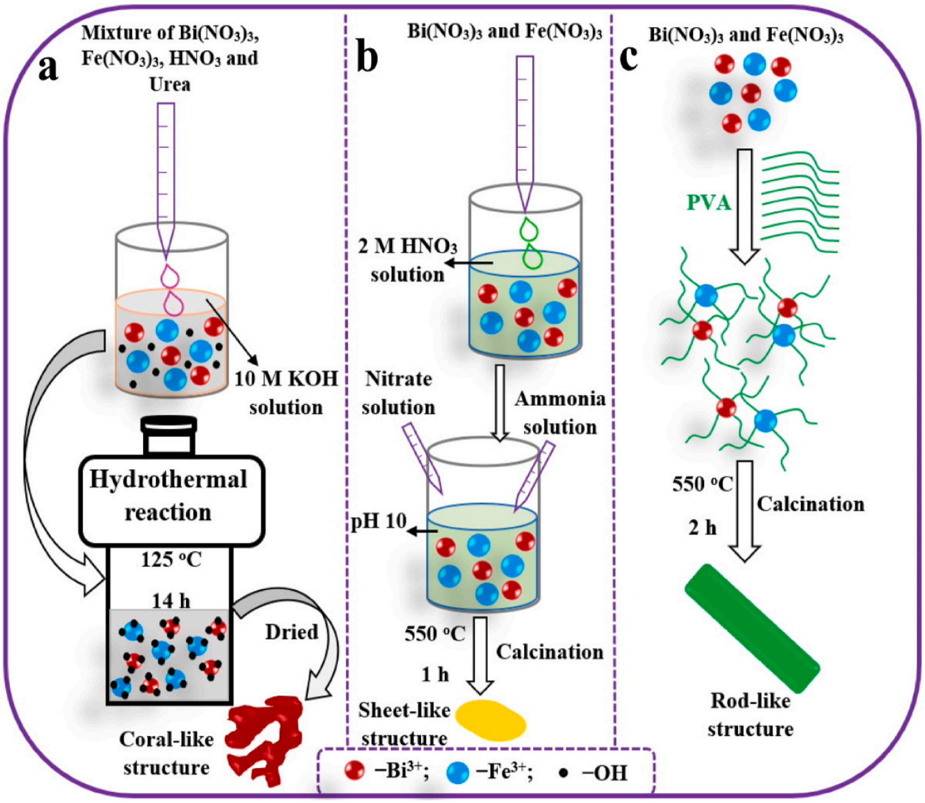

Fig. 1. Schematic illustration of the $BiFeO_3$ synthesis using three different synthesis routes (a) hydrothermal route, (c) co-precipitation technique, and (c) sol-gel synthesis.

Recently, various $BiFO_3$ morphologies, including spindle-like [20], wires [21], mesh, mat-shaped [22], nanotubes [23] and bowl-arrays [24], have been successfully synthesized using different methods. However, a comparison among the various synthesis routes of $BiFeO_3$ and their effects on photocatalytic performance is not well documented in the literature. Hence, it is essential to synthesize $BiFeO_3$ materials using different techniques to investigate their influence on morphology, optical, photoelectrochemical and photocatalytic properties.

In the current study, three synthesis techniques were applied to fabricate $BiFeO_3$ materials with various morphologies and the average particle sizes ranging from nanometer to micrometer. The physicochemical, optical and electrochemical properties of as-synthesized materials were determined using numerous techniques. Phenol was applied as a model organic pollutant to investigate the photocatalytic activities of the as-synthesized materials. Finally, the recycling potential and possible photocatalytic mechanism over $BiFeO_3$ material were studied through electrochemical measurements and hydroxyl radical and reactive species detection during the photodegradation process.

2. Experimental section

2.1. Synthesis of $BiFeO_3$

All the chemicals were of analytical grade obtained from Sigma Aldrich and applied directly without any additional processing. Fig. 1 displays the three different routes to synthesize single-phase perovskite $BiFeO_3$ samples with various shapes and particle sizes. In the hydrothermal route, the equal molar ratio of ferric nitrate ($Fe(NO_3)_3{\cdot}9H_2O$, 5 mmol, 98%) and bismuth nitrate ($Bi(NO_3)_3{\cdot}5H_2O$, 5 mmol, 98%) were dissolved in a 20 mL aqueous solution of nitric acid (HNO_3, 2 mL, 65%) and urea (0.1 mol, 99.5%) under magnetic stirring. After 30 min of magnetic stirring, the whole mixture was inserted dropwise into a 10 M solution of potassium hydroxide (KOH, 85%) under strong magnetic stirring. The mixture was then shifted into a 100 mL Teflon-lined autoclave reactor for the hydrothermal reaction at 125 °C for 15 h. At the end of the reaction, the HT-$BiFeO_3$ particles were collected, washed with water/ethanol multiple times, and dried in an oven at 70 °C for 4 h.

In the co-precipitation (CP) method, equal molar $Bi(NO_3)_3{\cdot}5H_2O$ and $Fe(NO_3)_3{\cdot}9H_2O$ were dissolved in 2 M HNO_3 solution at room temperature. Both nitrate and ammonia solution were then added dropwise in the above mixture to maintain a solution pH of 10. The colloidal precipitate was settled through centrifugation and washed with ultrapure water until a solution pH of 7.0 was achieved. Afterward, the obtained particles were dried in an oven at 60 °C for 6 h. Finally, the dried particles were calcinated at 550 °C for 1 h to obtain the CP-$BiFeO_3$ sample.

In the sol-gel (SG) synthesis, 0.005 mol of $Bi(NO_3)_3{\cdot}5H_2O$ and 0.005 mol of $Fe(NO_3)_3{\cdot}9H_2O$ were dissolved into a 0.2 M aqueous HNO_3 solution. The above solution was then inserted into a 0.0025 M solution of polyvinyl alcohol (PVA) under strong magnetic stirring. The mixture was then heated at 60 °C until a gel was formed. The gel was then calcinated in a muffle furnace at 550 °C for 2 h to obtain the final SG-$BiFeO_3$ powder.

2.2. Characterizations

The crystalline structure of the synthesized products was investigated using X-ray diffraction (XRD, Rigaku D/Max 2550) at 40 kV, with Cu Kα as a source of radiation. The surface morphology of the samples was captured using a field emission scanning electron microscope (FESEM, JSM-6701 F). The elemental analysis was performed using energy dispersive X-ray (EDX) coupled with FESEM. The surface functional groups on the synthesized samples were recorded in the range between 400 and 4000/cm using Perkin Elmer Lambda 35. The absorption spectra of the samples were taken in the range of 200–800 nm using a PerkinElmer Lambda 750 S. The photoluminescence (PL) spectra were conducted at room temperature with 325 nm as excitation wavelength in a PerkinElmer S55. The magnetic properties were studied using the magnetic hysteresis (M − H, MicroSense 10 Mark II) loop.

2.3. Photoelectrochemical measurements

Photoelectrochemical measurements were performed in a three-electrode cell using 0.5 M sodium sulfate (Na_2SO_4, 99%) as an electrolyte. The fluorinated tin oxide (FTO) glass coated with the $BiFeO_3$ samples was applied as working electrodes. Silver chloride (Ag/AgCl) and platinum (Pt) wire acted as the reference and counter electrodes, respectively. The transient photocurrent response (TPR) spectra, Nyquist plot and linear sweep voltammetry (LSV) were investigated in a Gamry electrochemical workstation. Precisely, the photocurrent curve was investigated by controlling on-off light for 20 s with a bias voltage of 0.4V. The Nyquist plot was obtained at a frequency ranged between 0.1 Hz and 10 KHz. Finally, the LSV was executed at a scan rate of 50 mV/s.

2.4. Evaluation of photocatalytic test

For a typical reaction, 100 mg of the synthesized photocatalyst was dispersed in a 100 mL of 5 mg/L phenol aqueous solution to produce the reaction suspension. After the suspension was magnetically stirred for 30 min under dark conditions, it was exposed to direct sunlight irradiation with a light intensity of 875.4 W/m^2. As the photodegradation reaction proceeds, a certain volume of solution was taken from the reaction mixture, filtered using a 0.22 μm syringe filter to eliminate the photocatalyst particles. The filtered solution was then analyzed using a UV–vis spectrophotometer (*PerkinElmer Lambda 900 spectrometer*) at 270 nm wavelength. The chemical oxygen demand (COD) was investigated using COD vials incubated in a COD digester for 2 h at 150 °C. The phenol COD can be stoichiometrically calculated using the following phenol degradation reaction.

$$C_6H_5\mathrm{OH} + 6O_2 \rightarrow 6\mathrm{CO}_2 + 3H_2O \tag{1}$$

$$(\mathrm{COD})_{\mathrm{Phenol}} = [C]_{\mathrm{Phenol}} \times \frac{7 \times 32}{94.11} \tag{2}$$

where C is the concentration of phenol at a certain time. The COD of intermediated can be calculated using the following equation;

$$(\mathrm{COD})_{\mathrm{Intermediates}} = (\mathrm{COD})_{\mathrm{Total}} - (\mathrm{COD})_{\mathrm{Phenol}} \tag{3}$$

Additionally, the recycling potential of the SG-$BiFeO_3$ material was studied by executing six recycling reactions with 90 min for each run. At the end of each run, the photocatalytic material was magnetically separated from the solution, washed with distilled water and finally dried at 80 °C in an oven for a successive run. The dissolved Fe^{3+} ions concentration in the final solution was also investigated using inductive coupled plasma mass spectroscopy (ICP-MS).

2.5. Active species assessments

To examine the participation of reactive species in the photocatalytic reaction, triethanolamine (TEOA, 1 mM, h^+ scavenger), benzoquinone (BQ, 1 mM, quencher for superoxide radicals ($\bullet O_2^-$)), isopropyl alcohol (IPA, 1 mM, quencher for •OH) or catalyze (quencher for H_2O_2, 1 mM) was introduced into the phenol solution.

The amount of •OH radicals generated on the SG-$BiFeO_3$ sample was also measured using TAPL analysis [21]. Typically, 0.2 mM of terephthalic acid (TA, 99%) was ultrasonically dissolved in 100 mL of 0.025 mM sodium hydroxide (NaOH) solution. 0.1 g of prepared sample was added in the above solution and further sonicated for 1 h under dark conditions and then exposed to direct sunlight irradiation. The reacted solution was magnetically separated, and the TAPL spectra were recorded at 325 nm excitation wavelength using a spectrophotometer (PerkinElmer LS-55).

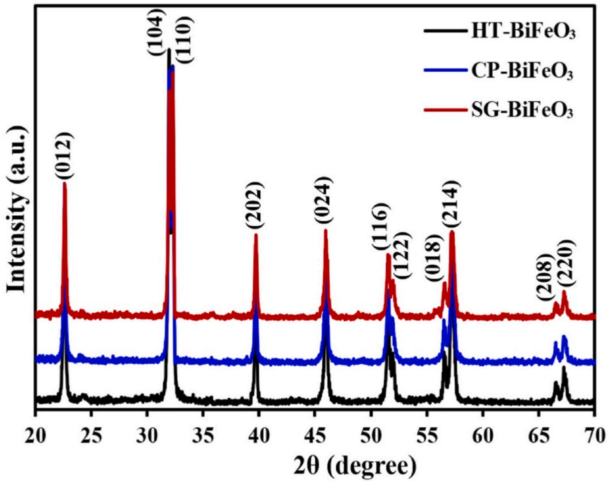

Fig. 2. XRD patterns of $BiFeO_3$ samples synthesized using different routes.

3. Results and discussion

3.1. Physiochemical characterizations

Fig. 2 depicts the XRD diffraction patterns obtained for the $BiFeO_3$ samples, namely HT-$BiFeO_3$, CP-$BiFeO_3$ and SG-$BiFeO_3$, synthesized using three different routes. All samples matched the rhombohedral perovskite structure of $BiFeO_3$ (JCPDS No. 20–0169) [25]. The strong and sharp peaks suggested that the as-synthesized $BiFeO_3$ materials were highly crystalline. **Additionally, no foreign characteristic peak for impurity was detected in the synthesized samples, indicating a high product purity.**

The morphology and elemental composition of the as-synthesized $BiFeO_3$ samples were investigated by FESEM and EDX analyses. The different fabrication routes induced dissimilar morphologies and particle sizes. The FESEM images showed that HT-$BiFeO_3$ (Fig. 3(a)) possesses a coral-like morphology with an average particle size around 130 nm, the CP-$BiFeO_3$ (Fig. 3(b)) had a sheet-like morphology with an average width and diameter of 10 nm and 150 nm, respectively, while SG-$BiFeO_3$ (Fig. 3(c)) had a rod-like structure with an average diameter of 350 nm and a length ranged between 1.5 and 2.5 μm. The elemental analysis (Fig. 3(d–f)) showed that all the $BiFeO_3$ samples were composed of Bi, Fe and O elements. The weak C peak in the spectra can be associated with the supporting carbon tape. The elemental distributions in $BiFeO_3$ samples using EDX mapping (Fig. 3(g–i)) showed that Bi, Fe and O elements were uniformly distributed throughout the samples, which could be helpful for the effective charge carrier separation/transfer.

The surface functional groups of $BiFeO_3$ samples were investigated with the FTIR technique. As displayed in Fig. 4, all the $BiFeO_3$ samples exhibited sharp absorption peaks around 450 cm^{-1} and 554 cm^{-1}, which could be originated from the Fe–O–Fe bending and Fe–O stretching mode of the FeO_6 octahedral perovskite, respectively [26–28]. The weak peak around 1620 cm^{-1} could be attributed to the –OH bending mode of physisorbed water on the surface of $BiFeO_3$, while the strong and broad absorption peak at 3410 cm^{-1} could be assigned to the O–H stretching mode of –OH group on the surface of the catalysts [29,30]. Primarily, it can be noticed that the SG-$BiFeO_3$ sample exhibited stronger intensities of O–H bending and stretching mode of –OH groups than that of the remaining $BiFeO_3$ samples (insert of Fig. 4). The presence of –OH group in large quantity ensures their effective photodegradation performance. The –OH group served as a key quencher for the photogenerated charge carriers that led to the generation of active •OH radical, which is highly conducive for organic pollutants degradation [4].

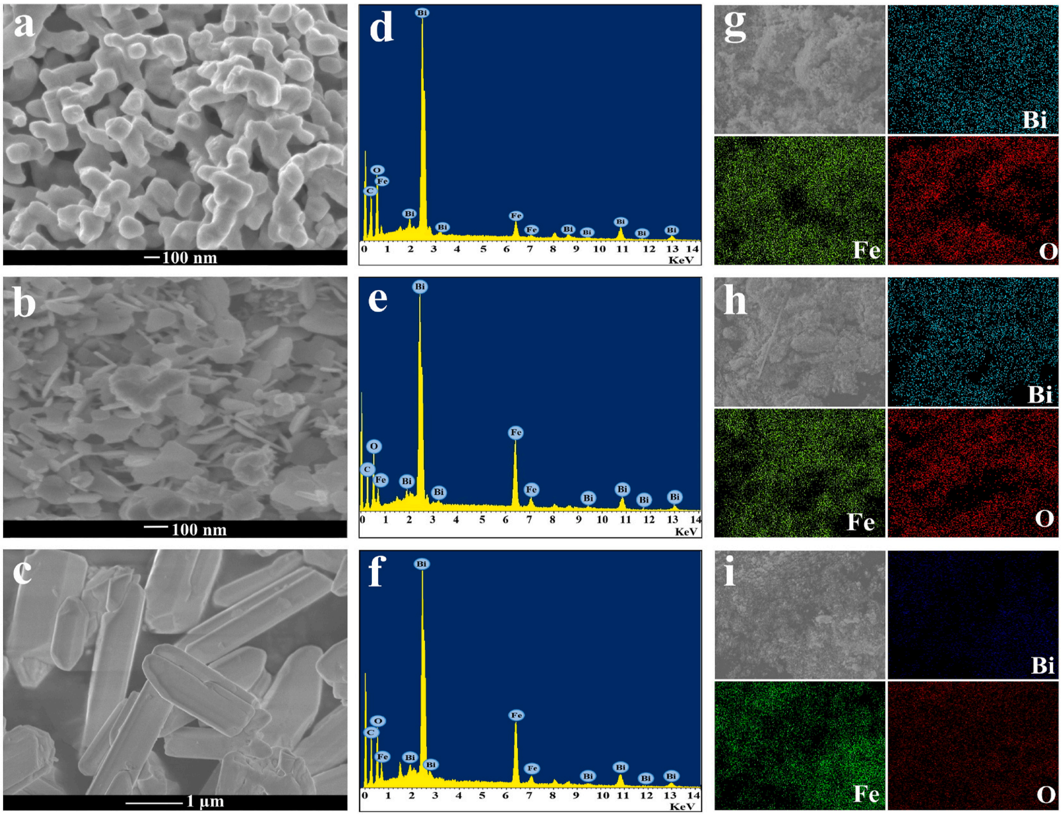

Fig. 3. FESEM images of the (a) HT-$BiFeO_3$, (b) CP-$BiFeO_3$ and (c) SG-$BiFeO_3$ samples; EDX analysis (d) CP-$BiFeO_3$, (e) HT-$BiFeO_3$ and (f) SG-$BiFeO_3$ samples; EDX mapping (g) CP-$BiFeO_3$, (h) HT-$BiFeO_3$ and (i) SG-$BiFeO_3$ samples.

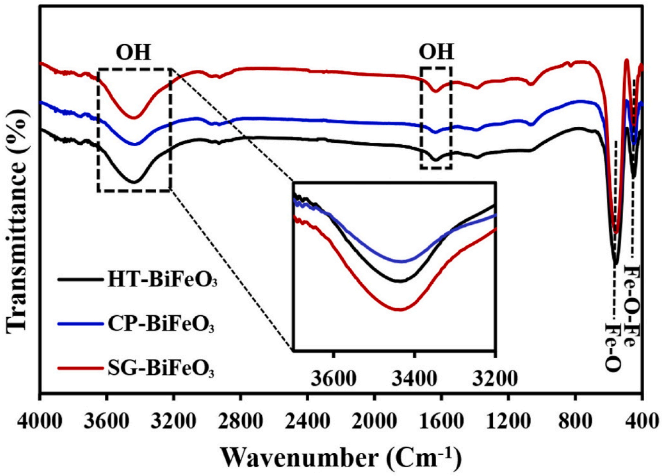

Fig. 4. FTIR spectra of $BiFeO_3$ samples synthesized using different routes.

3.2. Optical and electrochemical traits

Fig. 5(a) shows the optical absorption properties of the as-synthesized $BiFeO_3$ samples via three different synthesis routes. It can be seen that different synthesis routes can influence the optical properties of $BiFeO_3$. The SG-$BiFeO_3$ sample exhibited an absorption cut-off wavelength around 624 nm, which was higher than that of the HT-$BiFeO_3$ and CP-$BiFeO_3$ samples for absorption cut-off wavelength of 618 nm and 610 nm, respectively. The bandgap energies of $BiFeO_3$ samples can be estimated from the graph between $(\alpha h\nu)^2$ vs. energy bandgap (E_g) according to the well-known Kubelka-Munk (K-M) theory [31,32].

$$(\alpha h\nu)^2 = A(h\nu - E_g) \tag{4}$$

where α is the optical absorption, $h\nu$ is the photon energy, A is a constant, and E_g is the bandgap energy. The estimated bandgap energies for CP-$BiFeO_3$, HT-$BiFeO_3$ and SG-$BiFeO_3$ samples were around 2.12, 2.09 and 2.05 eV, respectively (Fig. 5(b)). The decline in the bandgap energies indicated that the SG-$BiFeO_3$ sample has more light absorption ability to facilitate the excitation of an electron from the valance band (VB) to the conduction band (CB), which might be advantageous for the photodegradation reaction. The CB and VB potential of $BiFeO_3$ can be calculated using the Mulliken electronegativity theory [33,34].

$$E_{VB} = X - E^e + 0.5E_g \tag{5}$$

$$E_{CB} = E_{VB} - E_g \tag{6}$$

where E_{CB}, E_{VB}, E_e, E_g and X are the conduction band potential, valance band potential, free electron energy on hydrogen scale (4.5 eV), bandgap energy of $BiFeO_3$ (eV) and absolute electronegativity of $BiFeO_3$, respectively. The absolute electronegativity value can be estimated using the following equation [34,35].

$$X(AmBnCl) = \sqrt[(m+n+1)]{X_A^m X_B^n X_C^1} \tag{7}$$

The absolute electronegativity values for Bi, Fe and O elements in $BiFeO_3$ were 4.69 eV, 4.04 eV and 7.54 eV, respectively [34]. Hence, the estimated $X_{(BiFeO3)}$ value from the above equation was 6.06 eV. After substituting these values in equations (5) and (6), the obtained E_{CB} and E_{VB} values were around 0.53 eV and 2.59 eV, respectively.

It is a well-known fact that the catalytic performance of a photocatalyst highly depended on the separation and transfer capabilities of photogenerated charge carriers. Therefore, a deep understanding of the dynamics of charge carriers on as-synthesized $BiFeO_3$ samples was a crucial issue. To interpret the insight into the generation of photogenerated charge carriers on $BiFeO_3$ samples, the PL emission of the

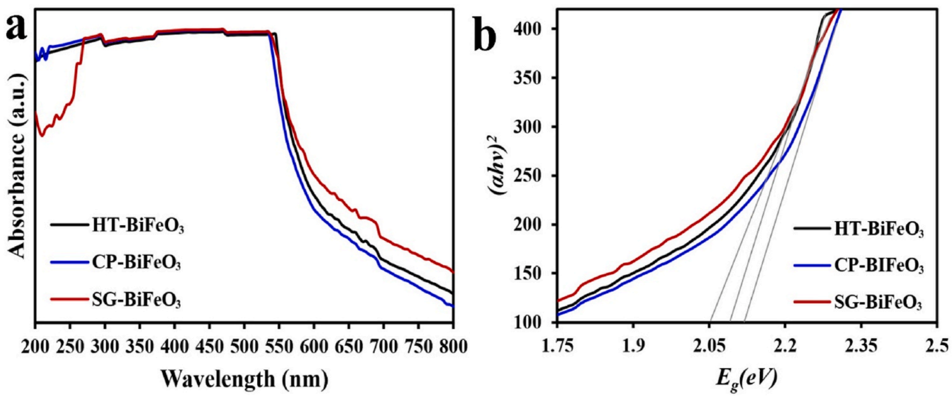

Fig. 5. UV–vis DRS spectra of various $BiFeO_3$ samples and (b) Plots of $(\alpha h\nu)^2$ vs. photon energy (E_g) of absorbed light for $BiFeO_3$ samples.

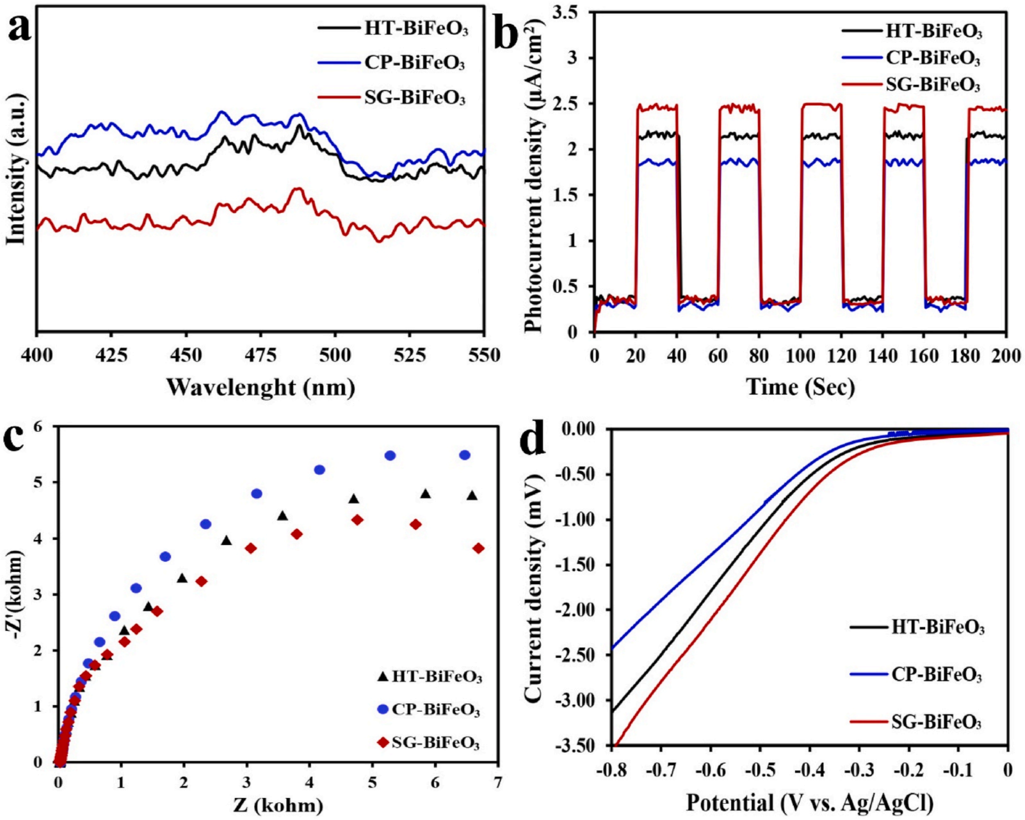

Fig. 6. (a) PL spectra, (b) TPR, (c) EIS Nyquist plot and (d) LSV of $BiFeO_3$ samples fabricated via different techniques.

synthesized samples were recorded. Fig. 6(a) depicts the PL spectra of $BiFeO_3$ samples synthesized using three different synthesis techniques. It can be seen that the PL intensity of the SG-$BiFeO_3$ sample was lower than that of the HT-$BiFeO_3$ and CP-$BiFeO_3$ sample, suggesting that the charge carrier's separation efficiency could be boosted using the sol-gel synthesis technique and thereby gave an ameliorated photocatalytic activity [7].

The TRP spectra is a common indicator to study the charge carrier separation efficiency on the photocatalyst surface. A superior photocurrent value means better charge carrier separation/transfer and higher photodegradation performance [36]. As illustrated in Fig. 6(b), the highest photocurrent intensity (2.49 μA/cm^2) was recorded using the SG-$BiFeO_3$ sample, which was 1.36 and 1.17 times higher than those of the HT-$BiFeO_3$ (1.82 μA/cm^2) and CP-$BiFeO_3$ (2.12 μA/cm^2) samples, respectively, signifying that the SG-$BiFeO_3$ had the least charge carrier recombination efficiency. Besides, electrochemical impedance (EIS) is also a vital indicator of the photogenerated charge carrier's separation and transfer capability on the photocatalyst surface. The smaller the arc radius in the impedance figure, the inferior the impedance posed by the material [34,36]. Fig. 6(c) shows the various synthesis routes highly affected the electrochemical impedance of $BiFeO_3$ samples. The smallest electrochemical impedance happened to the SG-$BiFeO_3$ sample (3.81 kΩ), which was only 0.79 and 0.69 times that of the HT-$BiFeO_3$ (4.78 kΩ) and CP-$BiFeO_3$ (5.5 kΩ), respectively, indicating that the SG-$BiFeO_3$ sample owned the best charge carrier's separation efficiency. Moreover, the LSV spectra were also performed to investigate the photoelectrochemical properties of synthesized samples further. As shown in Fig. 6(d), the lowest overpotential and maximum photocurrent density of SG-$BiFeO_3$ sample suggested that it can appropriately enhance photogenerated charge carrier separation and transfer than the remaining

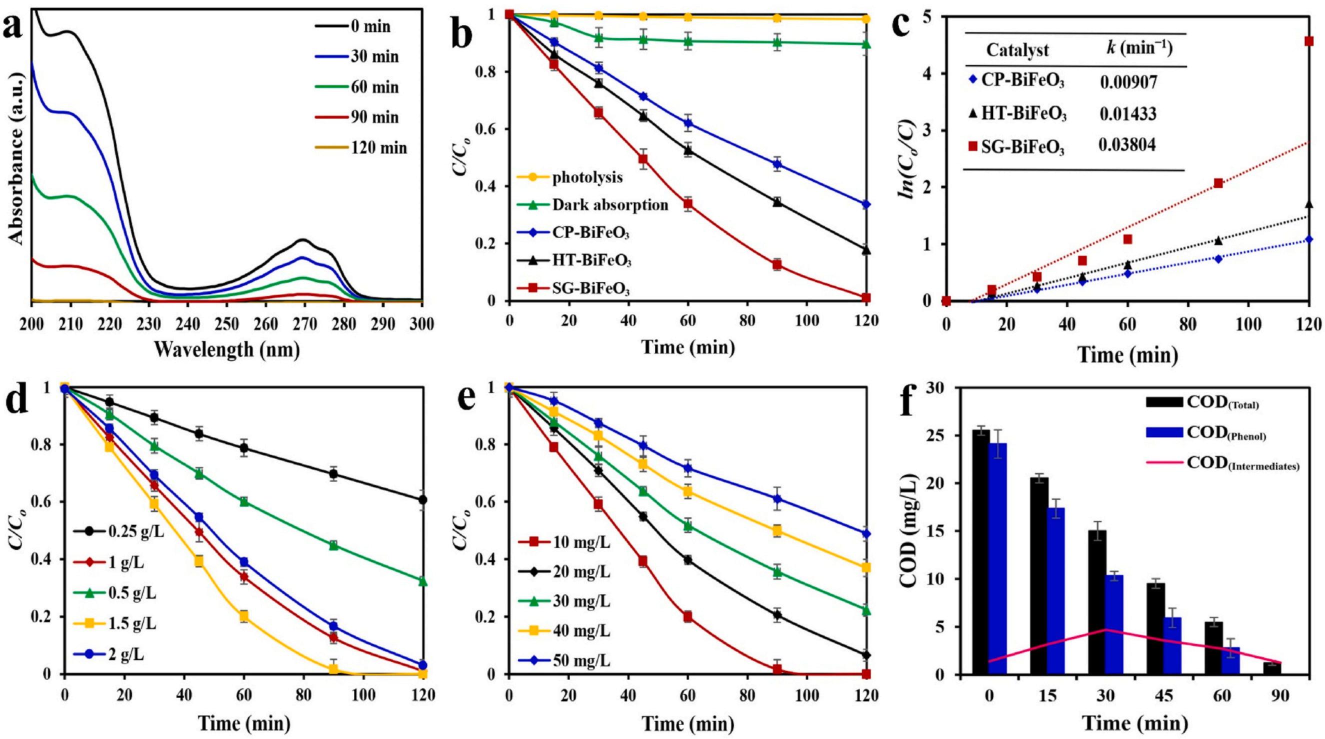

Fig. 7. UV–vis absorption spectra of phenol degradation with various direct sunlight irradiation time over SG-BiFeO$_3$, (b) photocatalytic degradation of phenol over photolysis, dark absorption and various BiFeO$_3$ samples under direct sunlight irradiation, (c) corresponding pseudo-first-order plots and rate constant *k* values over numerous samples, (d) effect of photocatalyst loading on the phenol degradation over SG-BiFeO$_3$, (e) effect of initial substrate concentration on photodegradation of phenol using SG-BiFeO$_3$ and (f) COD variations versus time.

two samples. The LSV analysis was in accordance with the UV–vis DRS, PL, TPR and EIS findings, which further confirm that the SG-BiFeO$_3$ sample can show effective charge carrier separation, thus, the highest photocatalytic performance.

3.3. Photocatalytic degradation of phenol

The photodegradation performance of differently synthesized BiFeO$_3$ samples was estimated against the degradation of phenol solution under direct sunlight irradiation. Before the sunlight irradiation, the suspension was stirred under dark conditions to attain an adsorption-desorption equilibrium state. Fig. 7(a) depicts the absorption spectra of phenol solution obtained at 30 min intervals in the existence of the SG-BiFeO$_3$ sample. The main absorption peak of phenol was situated around 270 nm, whose intensity dropped rapidly with the rise in light irradiation time. After 120 min of sunlight irradiation, the peak almost became a flat line, suggesting a complete degradation of phenol molecules.

Fig. 7(b) shows the changes in C/C_o vs. time for the photolysis, dark absorption and photodegradation tests in the existence of CP-BiFeO$_3$, HT-BiFeO$_3$ and SG-BiFeO$_3$ samples. The comparative studies suggested that when the phenol solution was irradiated in the absence of BiFeO$_3$ samples or when the phenol solution in the presence of SG-BiFeO$_3$ sample was stirred under the dark conditions, an insignificant amount of phenol was eliminated. In the existence of BiFeO$_3$ samples, the direct sunlight irradiation for 120 min resulted in a 66.9% and 77.4% phenol degradation using CP-BiFeO$_3$ and HT-BiFeO$_3$ samples, respectively. In contrast, the SG-BiFeO$_3$ particles led to a 98.95% phenol degradation after a similar duration of sunlight irradiation. The superior photodegradation performance of BiFeO$_3$ particles could be attributed to the smaller energy bandgap and well-defined rod-like morphology, which could reduce the photogenerated charge carrier recombination and enhance the number of active sites on the photocatalyst surface. The photocatalytic degradation was best suited for the pseudo-first-order kinetics, and the rate constant (*k*) was corresponding to the line slope (Fig. 7(c)). As can be seen that the *k* values of SG-BiFeO$_3$, HT-BiFeO$_3$ and CP-BiFeO$_3$ samples were 0.03804/min, 0.01433/min and 0.00907/min, respectively. The SG-BiFeO$_3$ sample showed the highest *k* value for phenol degradation, which was around 2.65 and 4.19 times higher than that of the HT-BiFeO$_3$ and CP-BiFeO$_3$ samples, respectively. Hence, the SG-BiFeO$_3$ sample was then chosen for the following experiments.

3.3.1. Effect of catalyst dosage

The effect of SG-BiFeO$_3$ dosage on the photodegradation reaction was investigated, and results are presented in Fig. 7(d). When SG-BiFeO$_3$ dosage was increased from 0.25 g/L to 1.5 g/L, the photocatalytic degradation of phenol was increased from 40.95% to 100%. However, further enhancement in SG-BiFeO$_3$ dosage to 2.0 g/L caused a decreasing efficiency to 86.4%. At a lower catalyst dosage, the catalyst absorbs fewer photons to initiate the photodegradation reaction, thus lower photocatalytic performance. Upon enhancing the catalyst dosage, the number of active sites and light absorption centers on the catalyst surface also increased, thereby improving the photocatalytic performance [37]. Besides, the optimized catalyst dosage can also enhance the generation of photogenerated charge carriers, which led to an enhancement in the production of reactive radical species. Nonetheless, when the catalyst dosage was enhanced beyond the optimum amount, the limited light diffusion into the suspension and enhanced solution turbidity led to a decline in the photocatalytic degradation performance [34,38]. Hence, 1.5 g/L catalyst dosage was selected in the following study.

3.3.2. Effect of initial concentration

To investigate the effect of initial phenol concentration on the SG-BiFeO$_3$ photocatalytic degradation, the photocatalytic trials were repeated by altering the initial phenol concentration from 10 mg/L to

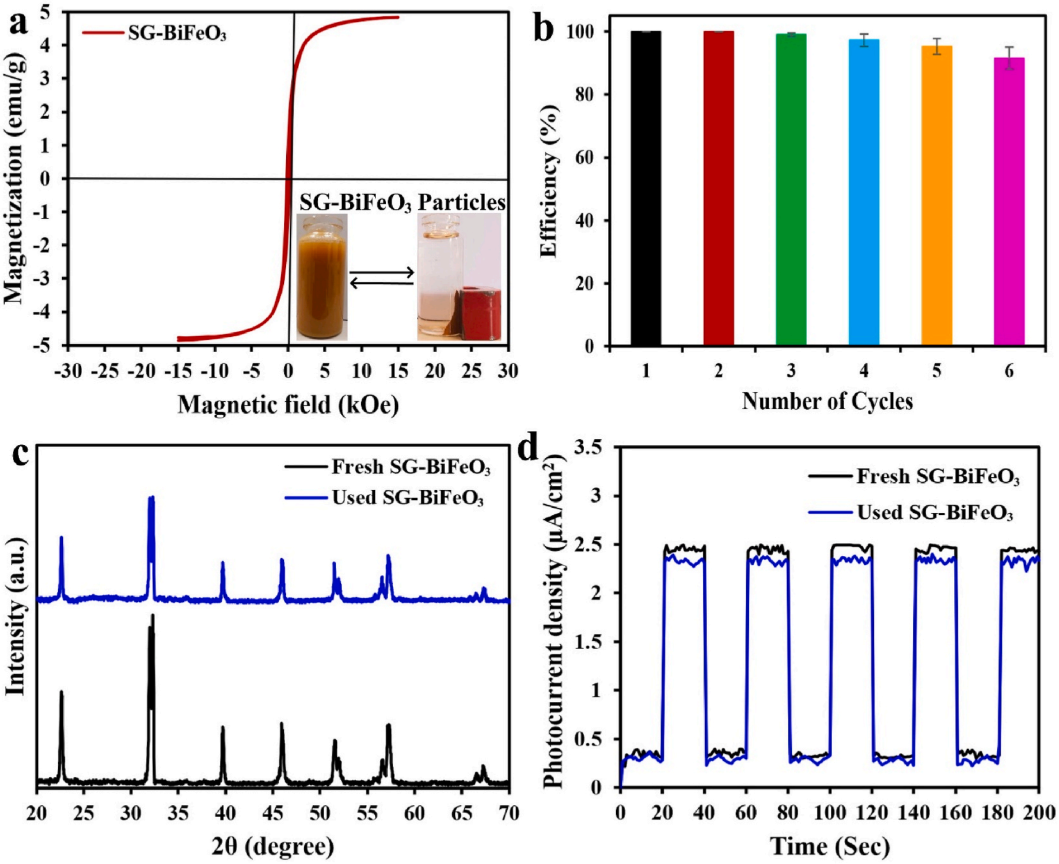

Fig. 8. M − H loop of SG-BiFeO$_3$ sample, insert of the figure is the magnetic separation of SG-BiFeO$_3$, (b) Six consecutive recycling runs in the photocatalytic degradation of phenol under direct sunlight irradiation, (c) XRD patterns of recycled and fresh SG-BiFeO$_3$ sample and (d) TPR comparison among the fresh and recycled SG-BiFeO$_3$ samples.

50 mg/L (Fig. 7(e)). A decline in photocatalytic degradation from 100% to 54.9% was recorded upon increasing the initial phenol concentration from 10 mg/L to 50 mg/L. The highest and lowest photodegradation rates were recorded at 10 mg/L and 50 mg/L, respectively. The decline in photodegradation efficiency at higher phenol concentration could be credited to the decrease in photocatalytic active sites accessibility to the phenol molecules, which ultimately led to a decline in reactive species generation to partook in photodegradation reaction [39,40]. Another possible reason for declined photodegradation performance could be due to the higher light absorption by phenol molecules than that of the SG-BiFeO$_3$ [40].

3.3.3. Chemical oxygen demand (COD) measurements

The intermediate products generated via partial oxidation of organic pollutants might lead to competitive adsorption on the photocatalyst surface or become more harmful than the initial one [41]. Hence, it was crucial to study the complete oxidation through the investigation of COD contents. It can be seen from Fig. 7(f), the total COD and COD of phenol decreased gradually as the reaction proceeds. In contrast, the concentration of reaction intermediates increased initially and then decreased until the photocatalytic reaction.

The photodegradation caused decomposition and ring-opening of phenol molecules resulted in the intermediate product generation, which ultimately mineralized into carbon dioxide (CO_2) and water (H_2O) [42]. When the phenol concentration decreased, an excess amount of reactive species and surface-active sites became available to facilitate the remaining phenol molecules and possible intermediate products. Consequently, around 95.05% reduction in total COD was recorded after 90 min of direct sunlight irradiation.

3.4. Magnetic properties and cyclic photodegradation

Fig. 8(a) illustrates the M − H loops of the synthesized SG-BiFeO$_3$ sample. The M − H loops displayed negligible coercivity and remanence magnetization in the absence of an external magnetic field, indicating the superparamagnetic nature of the synthesized sample [40]. Unlike other magnetic materials, superparamagnetic materials could be extremely useful in environmental applications due to their reversible magnetic interaction. When the external applied magnetic field was removed, the magnetic moment vanished, and the SG-BiFeO$_3$ particles were redispersed in the aqueous solution (inset of Fig. 8(a)), thus establishing the prospect of their recycling properties. A clear specific saturation magnetization of about 4.91 emu/g was recorded, which was higher than that of the reported BiFeO$_3$ literature [43–45].

Fig. 8(b) depicts the photocatalytic stability of the SG-BiFeO$_3$ sample for six consecutive runs against phenol degradation. At the end of each run, the SG-BiFeO$_3$ particles were collected using a small external magnet, washed, dried and reused in fresh phenol solution degradation. A slight decline in the photocatalytic performance was recorded. At the end of the sixth run, the SG-BiFeO$_3$ sample still showed more than 92% degradation efficiency. In the current study, Fe^{3+} ion leaching during recycling tests was also verified using the ICP-MS technique. It found that no Fe^{3+} ion leaching was detected, proving the high stability of the photocatalytic material. These findings were also consistent with other BiFeO$_3$-based literature reports [11,15].

To further confirm the stability of photocatalyst, XRD and TPR analyses of the recycled SG-BiFeO$_3$ were performed. Fig. 8(c) depicts the XRD patterns of SG-BiFeO$_3$ before and after six cycles, confirming that there were no noticeable changes in XRD patterns. Moreover, Fig. 8(d) shows the TPR comparison among the fresh and used SG-BiFeO$_3$

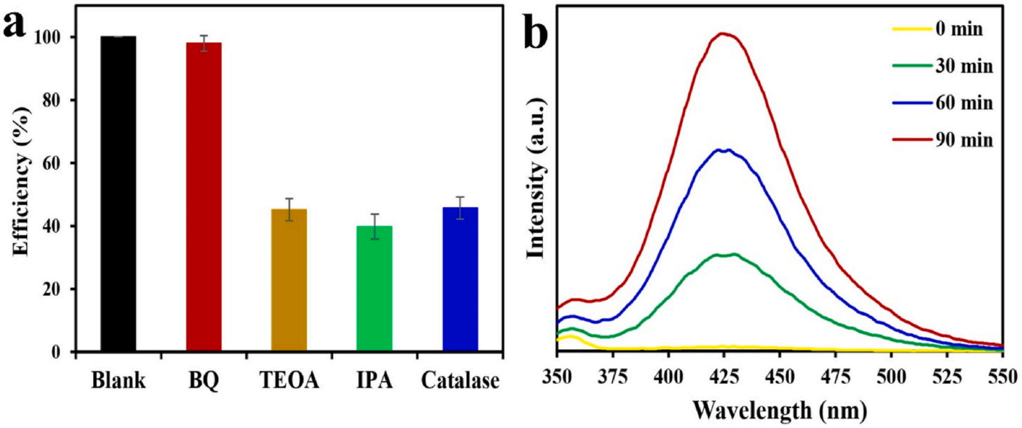

Fig. 9. Effect of different radical scavengers on phenol degradation using SG-$BiFeO_3$ sample and (b) TA-PL spectral changes with irradiation time for SG-$BiFeO_3$ sample in aqueous TA solution.

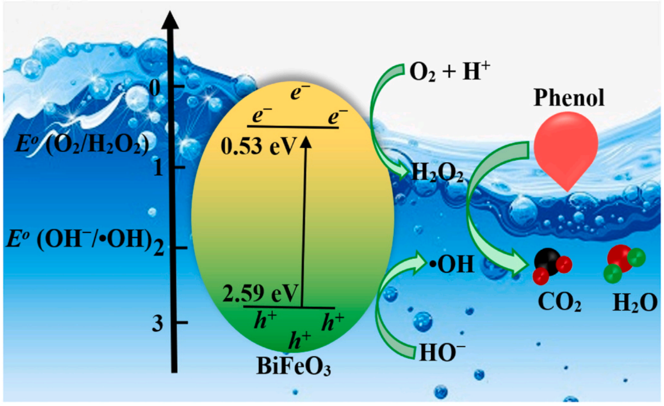

Fig. 10. Schematic diagram of direct sunlight photocatalytic degradation mechanism of $BiFeO_3$ sample.

samples. The results suggested that both the TPR intensities were almost similar over the six runs, proving high stability and an ideal candidacy of SG-$BiFeO_3$ material for continuous wastewater treatment.

3.5. Reasonable photodegradation mechanism

Identifying the prominent reactive species during the photodegradation reaction is essential for proposing the photocatalytic mechanism. Hence, it is imperative to perform a radical scavenging study. Herein, we applied 1 mM of TEOA, BQ, IPA, and catalyze as scavengers for h^+, $•O_2^-$, •OH and H_2O_2, respectively [7,46]. From Fig. 9 (a), it can be seen that the addition of BQ had a lesser effect on phenol degradation. In contrast, the addition of TEOA, IPA and catalase led to a dramatic decrease in phenol degradation to 45.2%, 39.8% and 45.7%, respectively, suggesting that the h^+, •OH, and H_2O_2 were the dominant reactive species. The active role of •OH radical was further investigated by the TAPL analysis. Literature reports suggested that the •OH radicals can react with the aqueous TA molecules to generate a highly fluorescent 2-hydroxyterephthalic acid (TA-OH) compound with a PL peak situated around 425 nm [22]. As shown in Fig. 9(b), no PL signal was recorded under dark conditions. Nonetheless, strong PL peaks for SG-$BiFeO_3$ were recorded after 30, 60 and 90 min of light irradiation, validating the •OH radicals were undoubtedly a key reactive species in phenol degradation reaction.

The above-stated results suggested that the SG-$BiFeO_3$ sample with a rod-like structure seems to have a higher photocatalytic degradation due to the generation of h^+, H_2O_2, and •OH radicals. The schematic charge transfer process and reactive oxidizing species generation for the SG-$BiFeO_3$ reaction are portrayed in Fig. 10. Under direct sunlight

Table 1
A comparison of the previously reported literature on the organic pollutant degradation using $BiFeO_3$ with findings in the current study.

Synthesis route	Morphology	Energy bandgap (eV)	Pollutant and concentration	Catalyst loading (g/L)	Light source	Removal efficiency	Ref.
Sol-gel	Spherical shaped	2.21	Mordant Blue 9, 50 mg/L	1.0	Direct sunlight	77.5% within 180 min	[48]
Template-technique	Nanotubes	–	Methylene blue, 10 mg/L	0.5	Visible light	75% within 180 min	[23]
Hydrothermal	Nanosphere	2.1	Methyl orange, 10 mg/L	2.0	Simulated sunlight	78% within 90 min	[49]
Electrospinning technique	Nanofibers	2.1	Tetracycline hydrochloride, 10 mg/L	1.0	300W Xe lamp	74% within 120 min	[50]
Hydrothermal	Cube-like	2.1	Rhodamine B, 100 mg/L	1.0	300W Xe lamp	18.76% within 150 min	[28]
Electrospinning technique	Mesh shaped	2.39	Methylene blue, 10 mg/L	0.5	Direct sunlight	84.7% within 240 min	[22]
Co-precipitation	Sheet-like	2.12	Phenol, 10 mg/L	1.0	Direct sunlight	66.9% within 120 min	Current Study
Hydrothermal	Coral-like	2.09	Phenol, 10 mg/L	1.0	Direct sunlight	77.4% within 120 min	Current Study
Sol-gel	Rod-like	2.06	Phenol, 10 mg/L	1.0	Direct sunlight	98.95% within 120 min	Current Study

irradiation, the photogenerated electron on the $BiFeO_3$ surface would migrate from filled VB to CB band and leaving an equal number of holes in VB. These promoted CB electrons of $BiFeO_3$ (+0.53 eV) can react with the oxygen molecules to generate H_2O_2 molecules ($E^o(O_2/H_2O_2) = +0.695$ eV) [35,47]. Simultaneously, the holes situated in the VB band of $BiFeO_3$ (+2.59 eV) would react with the OH^- ($E^o(\bullet OH/OH^-) = +1.99$ eV) to generate the •OH radicals [46]. Subsequently, these h^+, H_2O_2 and •OH radicals progressively attacked the surface adsorbed phenol molecules and converted them into non-toxic mineralized products. Finally, Table 1 was assembled to compare the present work results with earlier reported literature on organic pollutants elimination using $BiFeO_3$ photocatalysts.

4. Conclusion

In this report, three $BiFeO_3$ morphologies, including sheet-like, coral-like, and rod-like structures, were successfully synthesized using three different synthesis routes and analyzed using numerous characterization techniques. The as-synthesized SG-$BiFeO_3$ sample with rod-like structure exhibited a superior phenol photodegradation compared with the HT-$BiFeO_3$ and CP-$BiFeO_3$ techniques was attributed to the lower energy bandgap value and higher separation of photogenerated charge carriers. The process parameters such as catalyst dosage and initial phenol concentration were also found to show their effects on phenol degradation. Additionally, the SG-$BiFeO_3$ sample still sustained higher photocatalytic activity and no Fe^{3+} ion leaking after six recycling runs. Based on the radical trapping test, h^+, H_2O_2 and •OH radicals were the vital reactive oxidizing species in the phenol photocatalytic degradation reaction. This study opened up some new avenues for synthesizing distinct magnetic semiconductor materials, which can be structurally tuned for the effective degradation of organic pollutants.

CRediT authorship contribution statement

Shui-Wen Chang Chien: Formal analysis, Methodology, Resources. **Ding-Quan Ng:** Writing-Editing & Review. **Dileep Kumar:** Writing-Editing & Review. **Sze-Mun Lam:** Resources. **Zeeshan Haider Jaffari:** Conceptualizations, Formal analysis, Methodology, Software, Writing-original draft.

Declaration of competing interest

The authors declare that they have no known competing financial interests or personal relationships that could have appeared to influence the work reported in this paper.

References

[1] Y. Li, Y. Li, L. Li, F. Ma, J. Li, W. Zhang, Succulent-like core–shell composite: synthesis of CdS coated with an ultrathin layer of TiO_2 and enhanced photocatalytic performance in the degradation of crystal violet and hydrogen production, J. Phys. Chem. Solid. 152 (2021) 109959.

[2] Z.H. Jaffari, S.M.A. Abuabdou, D.-Q. Ng, M.J.K. Bashir, Insight into two-dimensional MXenes for environmental applications: recent progress, challenges, and prospects, FlatChem 28 (2021) 100256.

[3] C. Karthikeyan, P. Arunachalam, K. Ramachandran, A.M. Al-Mayouf, S. Karuppuchamy, Recent advances in semiconductor metal oxides with enhanced methods for solar photocatalytic applications, J. Alloys Compd. 828 (2020) 154281.

[4] T. Wu, J. Li, M. Chang, Y. Song, Q. Sun, F. Wang, H. Zou, Z. Shi, Photoluminescence properties and photocatalytic activities of SiO_2@ TiO_2: Sm^{3+} nanomaterials, J. Phys. Chem. Solid. 149 (2020) 109775.

[5] H. Dong, X. Zhang, J. Li, P. Zhou, S. Yu, N. Song, C. Liu, G. Che, C. Li, Construction of morphology-controlled nonmetal 2D/3D homojunction towards enhancing photocatalytic activity and mechanism insight, Appl. Catal. B Environ. 263 (2020) 118270.

[6] H. Karimi-Maleh, B.G. Kumar, S. Rajendran, J. Qin, S. Vadivel, D. Durgalakshmi, F. Gracia, M. Soto-Moscoso, Y. Orooji, F. Karimi, Tuning of metal oxides photocatalytic performance using Ag nanoparticles integration, J. Mol. Liq. 314 (2020) 113588.

[7] S.-M. Lam, Z.H. Jaffari, J.-C. Sin, H. Zeng, H. Lin, H. Li, A.R. Mohamed, Insight into the influence of noble metal decorated on $BiFeO_3$ for 2, 4-dichlorophenol and real herbicide wastewater treatment under visible light, Colloids Surfaces A Physicochem. Eng. Asp. 614 (2021) 126138.

[8] Y. Zhang, Y. Yang, Z. Dong, J. Shen, Q. Song, X. Wang, W. Mao, Y. Pu, X. Li, Enhanced photocatalytic activity of Ba doped $BiFeO_3$ by turning morphologies and band gap, J. Mater. Sci. Mater. Electron. 31 (2020) 15007–15012.

[9] W. Mao, Q. Yao, Y. Fan, Y. Wang, X. Wang, Y. Pu, X. Li, Combined experimental and theoretical investigation on modulation of multiferroic properties in $BiFeO_3$ ceramics induced by Dy and transition metals co-doping, J. Alloys Compd. 784 (2019) 117–124.

[10] M. Chen, C. Guo, S. Hou, J. Lv, Y. Zhang, H. Zhang, J. Xu, A novel Z-scheme AgBr/Pg-C_3N_4 heterojunction photocatalyst: excellent photocatalytic performance and photocatalytic mechanism for ephedrine degradation, Appl. Catal. B Environ. 266 (2020) 118614.

[11] J. Yin, G. Liao, J. Zhou, C. Huang, Y. Ling, P. Lu, L. Li, High performance of magnetic $BiFeO_3$ nanoparticle-mediated photocatalytic ozonation for wastewater decontamination, Separ. Purif. Technol. 168 (2016) 134–140.

[12] G. Liu, S.K. Karuturi, H. Chen, D. Wang, J.W. Ager, A.N. Simonov, A. Tricoli, Enhancement of the photoelectrochemical water splitting by perovskite $BiFeO_3$ via interfacial engineering, Sol. Energy 202 (2020) 198–203.

[13] S.H. Han, K.S. Kim, H.G. Kim, H.-G. Lee, H.-W. Kang, J.S. Kim, C. Il Cheon, Synthesis and characterization of multiferroic $BiFeO_3$ powders fabricated by hydrothermal method, Ceram. Int. 36 (2010) 1365–1372.

[14] T. Gao, Z. Chen, Q. Huang, F. Niu, X. Huang, L. Qin, Y. Huang, A review: preparation of bismuth ferrite nanoparticles and its applications in visible-light induced photocatalyses, Rev. Adv. Mater. Sci. 40 (2015) 97–109.

[15] Z.H. Jaffari, S. Lam, J. Sin, H. Zeng, A.R. Mohamed, Magnetically recoverable Pd-loaded $BiFeO_3$ microcomposite with enhanced visible light photocatalytic performance for pollutant , bacterial and fungal elimination, Separ. Purif. Technol. 236 (2020) 116195.

[16] A.K. Pradhan, K. Zhang, D. Hunter, J.B. Dadson, G.B. Loiutts, P. Bhattacharya, R. Katiyar, J. Zhang, D.J. Sellmyer, U.N. Roy, others, Magnetic and electrical properties of single-phase multiferroic $BiFeO_3$, J. Appl. Phys. 97 (2005) 93903.

[17] M.H. Basiri, H. Shokrollahi, G. Isapour, Effects of La content on the magnetic, electric and structural properties of $BiFeO_3$, J. Magn. Magn Mater. 354 (2014) 184–189.

[18] B. Zhou, Y. Li, J. Bai, X. Li, F. Li, L. Liu, Controlled synthesis of rh-In_2O_3 nanostructures with different morphologies for efficient photocatalytic degradation of oxytetracycline, Appl. Surf. Sci. 464 (2019) 115–124.

[19] M. Karmaoui, L. Lajaunie, D.M. Tobaldi, G. Leonardi, C. Benbayer, R. Arenal, J. A. Labrincha, G. Neri, Modification of anatase using noble-metals (Au, Pt, Ag): toward a nanoheterojunction exhibiting simultaneously photocatalytic activity and plasmonic gas sensing, Appl. Catal. B Environ. 218 (2017) 370–384.

[20] Z.H. Jaffari, S. Lam, J. Sin, H. Zeng, Boosting visible light photocatalytic and antibacterial performance by decoration of silver on magnetic spindle-like bismuth ferrite, Mater. Sci. Semicond. Process. 101 (2019) 103–115.

[21] F. Gao, Y. Yuan, K.F. Wang, X.Y. Chen, F. Chen, J.-M. Liu, Z.F. Ren, Preparation and photoabsorption characterization of $BiFeO_3$ nanowires, Appl. Phys. Lett. 89 (2006) 102506.

[22] S. Bharathkumar, M. Sakar, V.K. R, S. Balakumar, Versatility of electrospinning in the fabrication of fibrous mat and mesh nanostructures of bismuth ferrite ($BiFeO_3$) and their magnetic and photocatalytic activities, Phys. Chem. Chem. Phys. 17 (2015) 17745–17754.

[23] X. Zhang, L. Chen, H. Sun, H. Zhang, W. Si, W. Wang, L. Wang, J. Li, others, Enhanced magnetic and photocatalytic properties of $BiFeO_3$ nanotubes with ultrathin wall thickness, Vacuum 184 (2021) 109867.

[24] X. Zhang, B. Wang, X. Wang, X. Xiao, Z. Dai, W. Wu, J. Zheng, F. Ren, C. Jiang, Preparation of M@$BiFeO_3$ nanocomposites (M= Ag, Au) bowl arrays with enhanced visible light photocatalytic activity, J. Am. Ceram. Soc. 98 (2015) 2255–2263.

[25] M. Humayun, A. Zada, Z. Li, M. Xie, X. Zhang, Y. Qu, F. Raziq, L. Jing, Enhanced visible-light activities of porous $BiFeO_3$ by coupling with nanocrystalline TiO_2 and mechanism, Appl. Catal. B Environ. 180 (2016) 219–226.

[26] H. Ramezanalizadeh, F. Manteghi, Immobilization of mixed cobalt/nickel metal-organic framework on a magnetic $BiFeO_3$: a highly efficient separable photocatalyst for degradation of water pollution, J. Photochem. Photobiol. A Chem. 346 (2017) 89–104.

[27] J. Wang, Y. Wei, J. Zhang, L. Ji, Y. Huang, Z. Chen, Synthesis of pure-phase $BiFeO_3$ nanopowder by nitric acid-assisted gel, Mater. Lett. 124 (2014) 242–244.

[28] C. Chun, C. Ting, Study on carbon quantum dots/$BiFeO_3$ heterostructures and their enhanced photocatalytic activities under visible light irradiation, J. Mater. Sci. Mater. Electron. 28 (2017) 10019–10027.

[29] P. Shahini, A.A. Ashkarran, Immobilization of plasmonic Ag-Au NPs on the TiO_2 nanofibers as an efficient visible-light photocatalyst, Colloids Surfaces A Physicochem. Eng. Asp. 537 (2018) 155–162.

[30] H. Abou, Y. Essamlali, O. Amadine, K. Daanoun, Green synthesis of Ag/ZnO nanohybrid using sodium alginate gelation method, Ceram. Int. 43 (2017) 13786–13790.

[31] F. Zhang, L. Shen, J. Li, Y. Zhang, G. Wang, A. Zhu, Room temperature photocatalytic deposition of Au nanoparticles on SnS_2 nanoplates for enhanced photocatalysis, Powder Technol. 383 (2021) 371–380.

[32] Z. Lin, J. Huang, A hierarchical $H_3PW_{12}O_{40}/TiO_2$ nanocomposite with cellulose as scaffold for photocatalytic degradation of organic pollutants, Separ. Purif. Technol. 264 (2021) 118427.

[33] K. Saravanakumar, R. Karthik, S.-M. Chen, J.V. Kumar, K. Prakash, V. Muthuraj, Construction of novel Pd/CeO_2/g-C_3N_4 nanocomposites as efficient visible-light photocatalysts for hexavalent chromium detoxification, J. Colloid Interface Sci. 504 (2017) 514–526.

[34] S.-M. Lam, Z.H. Jaffari, J.-C. Sin, H. Zeng, H. Lin, H. Li, A.R. Mohamed, D.-Q. Ng, Surface decorated coral-like magnetic $BiFeO_3$ with Au nanoparticles for effective sunlight photodegradation of 2,4-D and *E. coli* inactivation, J. Mol. Liq. 326 (2021) 115372.

[35] S. Chaiwichian, K. Wetchakun, W. Kangwansupamonkon, N. Wetchakun, Novel visible-light-driven $BiFeO_3$-Bi_2WO_6 nanocomposites toward degradation of dyes, J. Photochem. Photobiol. A Chem. 349 (2017) 183–192.

[36] R. Weng, F. Tian, Z. Yu, J. Ma, Y. Lv, B. Xi, Efficient mineralization of TBBPA via an integrated photocatalytic reduction/oxidation process mediated by MoS_2/$SnIn_4S_8$ photocatalyst, Chemosphere 285 (2021) 131542.

[37] A. Krishnan, P.V. Vishwanathan, A.C. Mohan, R. Panchami, S. Viswanath, A. V Krishnan, Tuning of photocatalytic performance of CeO_2-Fe_2O_3 composite by Sn-doping for the effective degradation of methlene blue (MB) and methyl orange (MO) dyes, Surfaces and Interfaces 22 (2021) 100808.

[38] D. Zhang, S. Lv, Z. Luo, A study on the photocatalytic degradation performance of a $[KNbO_3]_{0.9}$-$[BaNi_{0.5}Nb_{0.5}O_{3-\delta}]_{0.1}$ perovskite, RSC Adv. 10 (2020) 1275–1280.

[39] S. Juntrapirom, S. Anuchai, O. Thongsook, S. Pornsuwan, P. Meepowpan, P. Thavornyutikarn, S. Phanichphant, D. Tantraviwat, B. Inceesungvorn, Photocatalytic activity enhancement of g-C_3N_4/BiOBr in selective transformation of primary amines to imines and its reaction mechanism, Chem. Eng. J. 394 (2020) 124934.

[40] S. Raha, M. Ahmaruzzaman, Enhanced performance of a novel superparamagnetic g-C_3N_4/NiO/ZnO/Fe_3O_4 nanohybrid photocatalyst for removal of esomeprazole: effects of reaction parameters, co-existing substances and water matrices, Chem. Eng. J. 395 (2020) 124969.

[41] M. Jafarikojour, B. Dabir, M. Sohrabi, S.J. Royaee, Application of a new immobilized impinging jet stream reactor for photocatalytic degradation of phenol: reactor evaluation and kinetic modelling, J. Photochem. Photobiol. A Chem. 364 (2018) 613–624.

[42] S. Madadi, R. Biriaei, M. Sohrabi, S.J. Royaee, Photodegradation of 4-nitrophenol using an impinging streams photoreactor coupled with a membrane, Chem. Eng. Process. Process Intensif. 99 (2016) 1–9.

[43] S. Cheng, Q. Xu, X. Hao, Z. Wang, N. Ma, P. Du, Formation of nano-Ag/$BiFeO_3$ composite thin film with extraordinary high dielectric and effective ferromagnetic properties, J. Mater. Sci. Mater. Electron. 28 (2017) 5652–5662.

[44] L. Gong, Z. Zhou, S. Wang, B. Wang, Preparation and characterization of $BiFeO_3$@Ce-doped TiO_2 core-shell structured nanocomposites, Mater. Sci. Semicond. Process. 16 (2013) 288–294.

[45] P.C. Sati, M. Kumar, S. Chhoker, Raman spectroscopy and enhanced magnetic and dielectric properties of Pr and Ti codoped $BiFeO_3$ ceramics, J. Mater. Sci. Mater. Electron. 26 (2015) 530–538.

[46] Y. Chen, P. Zhu, M. Duan, J. Li, Z. Ren, P. Wang, Fabrication of a magnetically separable and dual Z-scheme PANI/Ag_3PO_4/$NiFe_2O_4$ composite with enhanced visible-light photocatalytic activity for organic pollutant elimination, Appl. Surf. Sci. 486 (2019) 198–211.

[47] L. Di, H. Yang, T. Xian, X. Chen, Enhanced photocatalytic degradation activity of $BiFeO_3$ microspheres by decoration with g-C_3N_4 nanoparticles, Mater. Res. 21 (2018).

[48] J. Ćirković, A. Radojković, D.L. Golić, N. Tasić, M. Čizmić, G. Branković, Z. Branković, Visible-light photocatalytic degradation of Mordant Blue 9 by single-phase $BiFeO_3$ nanoparticles, J. Environ. Chem. Eng. 9 (2021) 104587.

[49] Y. Li, X.-T. Wang, X.-Q. Zhang, X. Li, J. Wang, C.-W. Wang, New hydrothermal synthesis strategy of nano-sized $BiFeO_3$ for high-efficient photocatalytic applications, Phys. E Low-Dimens. Syst. Nanostruct. 118 (2020) 113865.

[50] Y. Ma, P. Lv, F. Duan, J. Sheng, S. Lu, H. Zhu, M. Du, M. Chen, Direct Z-scheme Bi_2S_3/$BiFeO_3$ heterojunction nanofibers with enhanced photocatalytic activity, J. Alloys Compd. 834 (2020) 155158.